Nanoscale Advances

ROYAL SOCIETY OF CHEMISTRY

PAPER

View Article Online
View Journal | View Issue

Cite this: *Nanoscale Adv.*, 2025, **7**, 1195

Photocatalytic CO_2 reduction of $Ag/Ag_2S/Ti_3C_2T_X$ heterojunctions with enhanced interfacial charge transfer†

Bo Zhang,[ab] Yijun Chen,[c] Fei Li,*[bd] Yang Zhang,[a] Xiang Li,[a] Wuwan Xiong *[a] and Weili Dai[e]

Photocatalytic reduction of CO_2 to produce organic fuels is a promising strategy for addressing carbon reduction and energy scarcity. Transition metal carbides ($Ti_3C_2T_X$) are of particular interest due to their unique layered structures and excellent electrical conductivity. However, the practical application of $Ti_3C_2T_X$ is limited by the poor separation efficiency of photogenerated charge carriers and the low migration ability of photogenerated electrons. Herein, $Ag/Ag_2S/Ti_3C_2T_X$ heterojunctions were synthesized by depositing Ag/Ag_2S nanoparticles onto layered $Ti_3C_2T_X$ substrates using a combination of co-precipitation and photoreduction methods. Fluorescence spectra, UV diffuse reflection, and photoelectric chemical characterizations demonstrated that $Ag/Ag_2S/Ti_3C_2T_X$ heterojunctions provided effective channels for the reverse and synergistic migration of electrons and holes, leading to improved spatial separation. Notably, the Ag component in the composite acts as an electron acceptor and reactive center, significantly enhancing the migration ability of photogenerated electrons. The total alcohol yield over $Ag/Ag_2S/Ti_3C_2T_X$ (125.3 μmol $g_{catal.}^{-1}$) was 5.1 times higher than that on Ag_2S (24.7 μmol $g_{catal.}^{-1}$) and 2.1 times higher than on $Ti_3C_2T_X$ (60.7 μmol $g_{catal.}^{-1}$). This study offers valuable insights into designing efficient photocatalytic CO_2 reduction catalysts.

Received 21st November 2024
Accepted 20th December 2024

DOI: 10.1039/d4na00969j

rsc.li/nanoscale-advances

1 Introduction

The escalating consumption of fossil fuels exacerbates energy scarcity. Concurrently, the persistent combustion of fossil fuels contributes to a heightened concentration of CO_2 within the atmosphere, with the consequent greenhouse effect precipitating global climate alterations.[1–5] Strategies to diminish atmospheric greenhouse gases, particularly CO_2, whilst addressing energy deficiencies, have emerged as focal points of research.[6–9] Notably, CO_2, recognized as an economical and non-toxic C1 resource, possesses the potential to be transformed into an array of organic compounds, including alcohols, low carbon olefins, aldehydes, ethers, and esters, *via* diverse methodologies.[6,10] Its utilization as a raw material can simultaneously alleviate the greenhouse effect and provide solutions to energy crises. It is crucial to acknowledge that CO_2 exhibits considerable thermodynamic stability, boasting the highest oxidation state of carbon within its molecular structure. The dissociation energy of the C=O bond (~430 kJ mol^{-1}) surpasses that of C–H (~336 kJ mol^{-1}) and C–C (~750 kJ mol^{-1}) bonds. Consequently, the conversion of CO_2 necessitates prior activation, demanding an input of energy surpassing the dissociation threshold of the C=O bond.[11] Photocatalytic CO_2 reduction represents an emergent technique for decrementing CO_2 levels. Leveraging renewable solar energy, photocatalysts trigger the transformation of inert CO_2 molecules into valuable fuels or chemical entities. This approach, harnessing renewable and non-pollutive solar energy, facilitates carbon reclamation and is characterized by numerous benefits: elimination of supplementary reducing gases, assurance of a non-toxic procedure, absence of pollutant generation, facilitation of material reuse, simplification of reaction apparatus, and streamlined operational condition controls.[12]

$Ti_3C_2T_X$, a novel graphene-analogous material, is characterized by its superior electrical conductivity and unique layered configuration, rendering it particularly promising for exploration within the realm of photocatalytic CO_2 reduction.[2,13–17] This distinctive layered architecture facilitates the swift transit and segregation of photoinduced electron–hole pairs while offering numerous active sites conducive to photocatalysis. Nonetheless,

[a]College of Environmental and Chemical Engineering, Zhaoqing University, Zhaoqing, 526061, P. R. China. E-mail: 19860204540@163.com
[b]The Key Lab of Pollution Control and Ecosystem Restoration in Industry Cluster Ministry of Education, South China University of Technology, P. R. China
[c]School of Environment and Energy, South China University of Technology, Guangzhou 510006, P. R. China
[d]School of Environmental Science and Engineering, Sun Yat-Sen University, Guangzhou, 510275, P. R. China. E-mail: lifei68@mail.sysu.edu.cn
[e]Key Laboratory of Jiangxi Province for Persistent Pollutants Control and Resources Recycle, Nanchang Hangkong University, Nanchang 330063, P. R. China

† Electronic supplementary information (ESI) available. See DOI: https://doi.org/10.1039/d4na00969j

pristine $Ti_3C_2T_X$ exhibits certain limitations, including a propensity for the facile recombination of photoinduced electron–hole pairs. Peng *et al.* have demonstrated that (001) $TiO_2/Ti_3C_2T_X$ nanocomposites, synthesized *via* a straightforward hydrothermal approach, can significantly enhance photocatalytic efficacy.[18] In these composites, the integration of (001) TiO_2 nanoflakes within the stratified $Ti_3C_2T_X$ culminates in the formation of an interfacial heterostructure. Leveraging the elevated conductivity inherent to two-dimensional $Ti_3C_2T_X$ facilitates the segregation of photoinduced charge carriers at the $Ti_3C_2T_X$–TiO_2 interface, thereby mitigating electron–hole recombination. Empirical results underscore that $Ti_3C_2T_X$ can be adeptly engineered to construct heterojunction composite photocatalysts paired with semiconductors of corresponding energy bands. Such judicious pairing not only curtails the recombination of electron–hole pairs but also amplifies the CO_2 photoreduction efficiency.

Metal sulfides, characterized by their unique structures, exceptional properties, and narrow band gaps, readily absorb light and demonstrate catalytic activity. Owing to these attributes, they hold significant promise for applications spanning environmental remediation and energy generation among others.[19–22] Notably, silver sulfide (Ag_2S) possesses a minimal band gap of 0.92 eV, ensuring a high absorption rate of solar illumination coupled with robust photoelectric characteristics and chemical resilience.[23–26] The conduction band of Ag_2S is positioned at approximately −0.45 eV, while its valence band is around 0.38 V. Importantly, the conduction band's potential is more negative than the reduction thresholds required for converting CO_2 into methanol and ethanol, underscoring its potential in photocatalytic CO_2 reduction endeavors. Presently, Ag_2S is predominantly employed in realms such as photocatalytic degradation of contaminants, detoxification of heavy metals, and hydrogen evolution.[24,27] Nevertheless, standalone Ag_2S suffers from elevated electron–hole recombination rates and a marked propensity for aggregation during synthesis, which compromises its photocatalytic efficacy. Researchers have ascertained that the incorporation of suitable substrates during synthesis effectively circumvents Ag_2S aggregation.[28–30] Moreover, these substrates aid in the efficient segregation of photogenerated electrons and holes. Silver, endowed with a low Fermi energy level, frequently serves as an electron sink. Photogenerated electrons derived from silver-based composite systems can be conveyed to the silver matrix *via* the interfacial region.[31,32] Jiang *et al.* have conducted an exhaustive examination of the electronic configurations in four distinct chalcogenide-based silver catalysts.[33] Their findings elucidate that the positions of the conduction and valence bands, the migratory velocity of photoinduced charge carriers, and the overall photostability and catalytic proficiency of these materials are governed by the band gap dimensions and the alignment of their respective bands. Consequently, the selection of catalysts for specific photocatalytic transformations varies accordingly.

To inhibit the recombination of photogenerated carriers in $Ti_3C_2T_X$ layered materials and enhance the number of photogenerated electrons with strong reducing capabilities for CO_2 photoreduction, the co-precipitation and photoreduction methods were employed to deposit Ag/Ag_2S onto $Ti_3C_2T_X$ in this study. The resulting compact heterojunction, formed by the amalgamation of Ag/Ag_2S with $Ti_3C_2T_X$, effectively prevented the recombination of electron–hole pairs. Upon photoexcitation, electrons with high reductive capabilities from the Ag_2S were efficiently transferred to the $Ti_3C_2T_X$ material *via* the heterojunction. Concurrently, photogenerated electrons, both from the $Ti_3C_2T_X$ material and Ag_2S transferred to the layered substrate, were directed to the metallic Ag with a low Fermi energy level. The synthesized $Ag/Ag_2S/Ti_3C_2T_X$ composites were then tested for photocatalytic CO_2 reduction, and their catalytic activity was evaluated. Additionally, the study explored how varying Ag_2S loadings affect the photocatalytic performance of the $Ag/Ag_2S/Ti_3C_2T_X$ composites.

2 Experimental sections

2.1 Preparation of $Ti_3C_2T_X$

$Ti_3C_2T_X$ materials were prepared using a procedure which is a modified recipe of the original version reported previously.[13,34] 1 g of Ti_3AlC_2 powders was added slowly into 10 mL of 40 wt% HF and etched at 25 °C for 36 h. The resulting precipitate was washed with deionized water and centrifuged at 8000 rpm for 5 min, that the pH of the supernatant was around 6. The samples after centrifuging were vacuum drying at 60 °C for 12 h.

2.2 Preparation of $Ag/Ag_2S/Ti_3C_2T_X$ composites

First, 0.1 g of layered $Ti_3C_2T_X$ was added into 40 mL of deionized water and stirred for 30 min. Then, 0.1 M $AgNO_3$ was injected into the solution and stirred for 1 h, sonicated for 15 min. Subsequently, 0.05 M $Na_2S{\cdot}9H_2O$ was slowly added and stirred for 2 h. Finally, the black precipitate obtained by exposure of xenon light for 30 min was washed several times with deionized water to remove the impurities on the surface and then dried at 80 °C for 12 h. The $Ag/Ag_2S/Ti_3C_2T_X$ composites with different mass ratio of Ag_2S and $Ti_3C_2T_X$ (6 wt%, 6.5 wt%, 7 wt%, 7.5 wt%, 8 wt%) was denoted as 6AAT, 6.5AAT, 7AAT, 7.5AAT, and 8AAT, respectively. In addition, pristine Ag_2S was synthesized *via* the above recipe in the absence of layered $Ti_3C_2T_X$ and photoreduction. And the $Ag_2S/Ti_3C_2T_X$ (mass ratio of Ag_2S and $Ti_3C_2T_X$ is 7.5 wt%, denoted as 7.5AT) was synthesized *via* the above recipe in the absence of photoreduction.

2.3 Characterizations

X-ray diffraction (XRD) measurements of the prepared catalytic materials were carried out on a powder diffractometer with instrument model D8 Advance X. Scanning electron microscopy (SEM) images were acquired on a Nova Nano SEM450 (FEI, USA) to observe the morphology and topography of the samples. Transmission electron microscopy (TEM) images were obtained on a JEM-2010F field emission electron microscope to characterize the morphological structure and high-resolution lattice fringes of the prepared photocatalysts, as well as the electron diffraction of the selected regions. X-ray photoelectron spectroscopy (XPS) analysis was performed on an Axis Ultra DLD to

obtain the data of the species and valence states of the elements, elemental content and chemical bonding in the prepared materials. UV-vis diffuse reflectance spectra (DRS) were recorded in a fluorescence spectrometer (LAMBDA950) equipped with an integrating sphere using $BaSO_4$ as the reference. Fourier transform infrared (FTIR) spectra were recorded on a Bruker Vertex 70 spectrometer to obtain characteristic bonding peaks between specific functional groups or elements. Photoluminescence spectroscopy (PL) was recorded on a F7000 fluorescence spectrometer (Hitachi, Japan). Specific surface areas and pore properties were measured using model TriStar-II to analyzed the specific surface area, pore size, and adsorption properties of the materials. Electrochemistry was used to study the conductive properties of photocatalytic materials and the transfer of electrons across material interfaces. Mott–Schottky and electrochemical impedance spectroscopy (EIS) measurements were performed on the electrochemical workstation (CHI660D) using graphite as the counter electrode, saturated calomel electrode as a reference electrode and the modified fluorine-doped tin oxide (FTO) glass as the working electrode. The electrolyte solution for the Mott–Schottky with transient photocurrent response was 0.5 M Na_2SO_4 solution.

2.4Photocatalytic CO_2 reduction tests

The efficiency of photocatalytic reduction of CO_2 was evaluated by the rate of catalytic reduction of CO_2 to organic alcohols under catalyst illuminated from a xenon lamp ($\lambda \geq 420$ nm). The catalyst (30 mg) was dispersed in 30 mL of deionized water at 4 °C. The reactor system was ensured that the reactants were only H_2O and CO_2 using the vacuum pump to remove gases such as air and dissolved O_2 from the device and aqueous solution. High-purity CO_2 (99.995%) was then introduced into the reactor without illumination for 0.5 h to obtain the saturated aqueous solution of CO_2 and followed by full-spectrum illumination for 4 h, where the sampling time interval was 1 h. The photoreduction generated products were detected through gas chromatograph (GC), and the yields of methanol and ethanol were calculated by standard curves of methanol and ethanol (Section S1, Table S1, and Fig. S1†).

3 Results and discussion

3.1 Structural and morphological characterizations

The crystalline phases of $Ti_3C_2T_X$, Ag_2S, and the $Ag/Ag_2S/Ti_3C_2T_X$ composites were characterized by analyzing their XRD patterns (Fig. 1a). All synthesized samples exhibited pronounced XRD diffraction peaks, suggesting a commendable degree of crystallinity.[13,18,35] Notably, several distinctive diffraction peaks at 25.9°, 28.9°, 31.5°, 34.3°, 36.8° for the singular Ag_2S material correspond to the planes of (−111), (111), (−112), (−121), and (121), respectively. These characteristic peaks matched well with JCPDS card no. 14-0072 for Ag_2S. Concurrently, the $Ti_3C_2T_X$ material manifested its characteristic diffraction peaks at 8.8° and 18.3°, indexing to the (002) and (004) crystal planes respectively, which matched with JCPDS card no. 52-0875. $Ag/Ag_2S/Ti_3C_2T_X$ composites were discerned that upon integrating

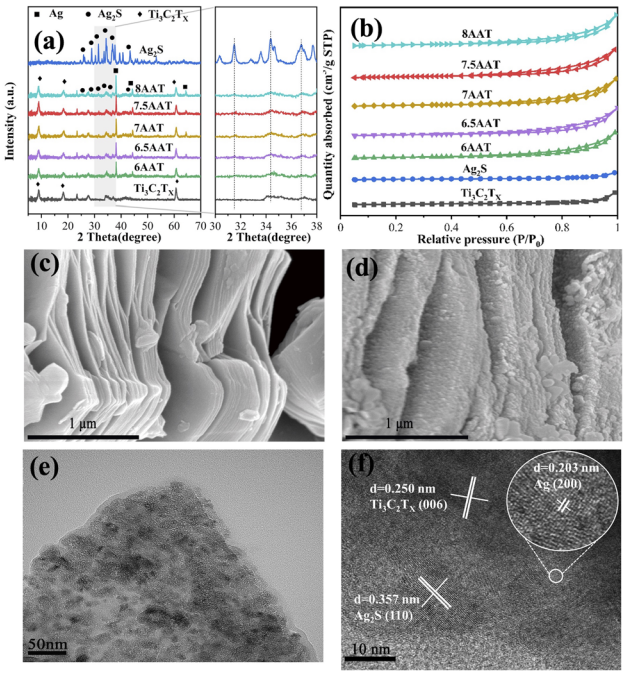

Fig. 1 XRD patterns (a) and N_2 adsorption–desorption curve (b) of Ag_2S, $Ti_3C_2T_X$, and $Ag/Ag_2S/Ti_3C_2T_X$ composites. SEM images of (c) $Ti_3C_2T_X$, (d) 7.5AAT composites. TEM (e) and HRTEM (f) images of 7.5AAT composites.

Ag and Ag_2S with $Ti_3C_2T_X$, which displayed the main structure $Ti_3C_2T_X$ with some signature peaks of Ag_2S materialized at 25.9°, 28.9°, 34.3° and 36.8°. Concurrently, the emergent peaks at 38.1°, 44.3°, and 64.4° were identified as the characteristic peaks of elemental Ag, correlating with the JCPDS card no. 04-0783. The overlaid XRD patterns elucidated that the $Ag/Ag_2S/Ti_3C_2T_X$ composites, irrespective of varying loadings retain analogous diffraction peaks to those of Ag, Ag_2S, and $Ti_3C_2T_X$. This observation was indicative of the fact that the amalgamation of Ag/Ag_2S with $Ti_3C_2T_X$ has not induced alterations in the crystalline configurations of either Ag_2S or $Ti_3C_2T_X$. Two augmentations in peak intensities corresponding to the (−112) and (−121) crystal planes of Ag_2S were observed with the Ag_2S loading progressively increased. Similarly, an enhancement in peak intensities at 38.1° related to the (111) crystal planes of Ag was noted. Cumulatively, these findings substantiate that both Ag and Ag_2S were adeptly integrated into the layered $Ti_3C_2T_X$ matrix without any resultant modifications to their crystal structures. N_2 adsorption–desorption analysis was conducted on the synthesized $Ti_3C_2T_X$, Ag_2S, and $Ag/Ag_2S/Ti_3C_2T_X$ composites, and the obtained curves were presented in Fig. 1b. The isotherms for $Ti_3C_2T_X$, Ag_2S, and $Ag/Ag_2S/Ti_3C_2T_X$ composites were characterized by Type IV isotherms with H3-type hysteresis loops, suggesting these materials exhibit mesoporous structures with slit-shaped pores.[13,26] Table 1 revealed that the specific surface areas for $Ti_3C_2T_X$, Ag_2S, 6AAT, 6.5AAT, 7AAT, 7.5AAT, and 8AAT measured 3.52, 4.48, 7.22, 7.50, 7.54, 8.06, and 8.2 $m^2\ g^{-1}$ respectively. Their average pore diameters stood at 15.62, 7.92, 16.12, 16.95, 16.62, 15.68, and 16.96 nm,

Table 1 BET surface area and porosity of samples

Sample	BET surface area (m^2 g^{-1})	Pore size (nm)	Pore volume (cm^3 g^{-1})
$Ti_3C_2T_X$	3.52	15.62	0.014
Ag_2S	4.48	7.92	0.009
6AAT	7.22	16.12	0.029
6.5AAT	7.50	16.95	0.032
7AAT	7.54	16.62	0.031
7.5AAT	8.06	15.68	0.032
8AAT	8.20	16.96	0.034

while the pore volumes were documented as 0.014, 0.009, 0.029, 0.032, 0.031, 0.32, and 0.034 cm^3 g^{-1}. Notably, upon compounding $Ti_3C_2T_X$ with Ag/Ag_2S, there was a marked enhancement in the specific surface area, pore volume, and pore size. The pore size (Fig. S2†) of $Ag/Ag_2S/Ti_3C_2T_X$ composites was increased in the range of 5–50 nm with increasing Ag_2S content. This phenomenon suggested that Ag/Ag2S particles were effectively anchored onto the $Ti_3C_2T_X$ substrate, leading to an augmented specific surface area and pore size. Such modification was beneficial for enhancing the interaction between the catalyst and the reactant, subsequently exposing a greater number of active sites.

SEM image of layered $Ti_3C_2T_X$ synthesized *via* the acid etching technique was shown in Fig. 1c, revealing the derived $Ti_3C_2T_X$ possesses a uniformly layered structure characterized by smooth and planar surfaces. The thickness of the $Ti_3C_2T_X$ layers varies between 50–100 nm. Notably, these layers predominantly consisted of two-dimensional nano-sheets separated by substantial pore spaces. This particular layered configuration enhanced the capacity for adsorbing gaseous CO_2 while concurrently offering an increased number of photoactive sites and shorter paths for photogenerated carrier transport, as referenced in literature.[36,37] As shown in Fig. 1d, the SEM image of the 7.5AAT composites revealed that the fundamental laminar architecture remained unaltered post-incorporation of Ag/Ag_2S with the comparison with pristine $Ti_3C_2T_X$, suggesting that the Ag/Ag_2S integration did not compromise the inherent lamellar structure of $Ti_3C_2T_X$. Moreover, $Ag/Ag_2S/Ti_3C_2T_X$ surface hosted numerous particles with an approximate diameter of 25 nm, dispersed uniformly across its smooth plane. This observation confirmed that following the co-precipitation and photo-reduction procedures, Ag/Ag_2S particles were securely anchored onto the $Ti_3C_2T_X$ layers without any noticeable aggregation. TEM and High-Resolution Transmission Electron Microscopy (HRTEM) images of the 7.5AAT composite were conducted. TEM image in Fig. 1e underscored the layered disposition adorned with a copious loading of particle substances on its exterior, aligning with SEM findings. HRTEM image in Fig. 1f allows for the precise measurement of the lattice fringes with *a* spacing of 0.203 nm, 0.250 nm, and 0.357 nm, indexing to the (200) plane of metallic Ag, the (006) plane of $Ti_3C_2T_X$, and the (110) plane of Ag_2S, respectively.[18,29,38] These measurements affirmed the establishment of a densely packed heterojunction among $Ti_3C_2T_X$, Ag, and Ag_2S.

High-resolution XPS spectra with a Gaussian fitting process focusing on Ti 2p, C 1s, Ag 3d, and S 2p peaks were conducted. Specifically, Fig. 2a offers an in-depth view of the Ti 2p spectrum. Both $Ti_3C_2T_X$ and the 7.5AAT composite exhibited four distinct doublet peaks for Ti 2p. This spectrum was characterized by two primary energy levels, $2p_{3/2}$ and $2p_{1/2}$, maintaining an approximate area ratio of 2 : 1 and demonstrating an electron binding energy differential of approximately 5.7 eV. It is noted that the peaks located at 454.97, 455.68, 457.11, and 459.80 eV correspond to the Ti $2p_{3/2}$ energy level in the $Ti_3C_2T_X$ material, which are attributed to the titanium–carbon (Ti–C) bond, with the titanium–halide (Ti–X) bond associated with substoichiometric titanium carbide (TiC_x) or titanium-based oxycarbide, alongside the reduced states of titanium oxygen (Ti_xO_y) and the titanium–fluoride (Ti–F) bond. In comparison to the $Ti_3C_2T_X$ material, the peak positions associated with the reduced state Ti_xO_y of titanium (Ti) ions in the 7.5AAT composited remain consistent with the peak linked to the Ti $2p_{3/2}$ energy level in both the Ti–X bond and titanium oxycarbide. Notably, there was a discernible shift in the binding energy for the peak related to the Ti $2p_{3/2}$ energy level of the Ti–C bond in the 7.5AAT composite by 0.22 eV toward a lower value. Furthermore, an emergent Ti $2p_{3/2}$ energy level peak at 459.05 eV, corresponding to the titanium–oxygen (Ti–O) ionic bond, suggested alterations in the chemical environment surrounding the Ti–C bond subsequent to the amalgamation of $Ti_3C_2T_X$ with Ag/Ag_2S, resulting in partial oxidation of titanium-to-titanium dioxide (TiO_2).[18,34,35,39] The significant change in the relative intensity of the peaks in the Ti 2p spectra of the two samples also observed, which is attributed to partial oxidation of the $Ti_3C_2T_X$ surface during the loading of the catalytic materials. This process introduces Ti–O bonds, leading to variations in the Ti 2p peak intensities and shifts. It was imperative to note that TiO_2 exhibits photoresponse exclusively to ultraviolet light, demonstrating no responsiveness to illumination within the visible and near-infrared spectrum.[40] XPS

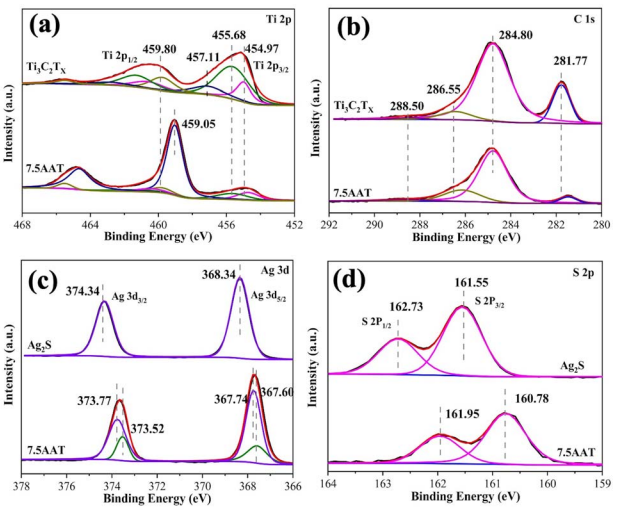

Fig. 2 High-resolution XPS spectra of (a) Ti 2p, (b) C 1s, (c) Ag 3d and (d) S 2p in Ag_2S, $Ti_3C_2T_X$, and $Ag/Ag_2S/Ti_3C_2T_X$ composites.

analysis of C 1s depicted in Fig. 2b to determine the binding energies of C 1s in its various forms. Within the $Ti_3C_2T_X$ material, the binding energies were identified as 281.77 eV, 284.80 eV, 286.55 eV, and 288.50 eV, corresponding to the C in Ti–C bond, C–C bond, C–O bond, and C–F bond, respectively. In the 7.5AAT material, there was a notable shift in the binding energy for C in the Ti–C bond and C–O bond, with decrease of 0.27 eV and 0.36 eV, respectively. In contrast, the binding energy associated with the C–F bond remained unchanged.[13] Fig. 2c presented a high-resolution scan of Ag 3d. The distinct peaks observed at 368.34 eV and 374.34 eV in Ag_2S align with the characteristic peaks of Ag $3d_{5/2}$ and Ag $3d_{3/2}$, respectively. This observation suggested that Ag within the Ag_2S material exhibited a valency of +1. For the 7.5AAT composite, the characteristic peaks for Ag $3d_{5/2}$ and Ag $3d_{3/2}$ of Ag^+ were positioned at 367.74 eV and 373.77 eV, respectively, revealing a significant offset of approximately 0.6 eV compared to the Ag_2S material. Furthermore, the characteristic peaks for 7.5AAT at 367.60 eV and 373.52 eV correspond to the Ag $3d_{5/2}$ and Ag $3d_{3/2}$ peaks of Ag, confirming the incorporation of metallic Ag within the composite material.[41] Fig. 2d presented a high-resolution scan of S 2p. The peaks located at 161.55 and 162.73 eV correspond to S $2p_{3/2}$ and S $2p_{1/2}$ of the S element in unadulterated Ag_2S,[30] respectively. These peaks denoted a valence state of −2 for the S element. Compared with pure Ag_2S, a notable shift to lower binding energies was observed for S $2p_{3/2}$ and S $2p_{1/2}$ in the 7.5AAT composite. Such findings suggested that upon the compounding of Ag/Ag_2S with $Ti_3C_2T_X$, the Ag/Ag_2S material became deposited atop the $Ti_3C_2T_X$ layered substrate, thereby forming a heterojunction. This recombination induced alterations in the chemical milieu of the constituent elements and precipitates an electron flux between the materials, which subsequently modified the binding energy of each element within the composite matrix. To quantitatively assess the proportions of Ag^0 and Ag^+ within the $Ag/Ag_2S/Ti_3C_2T_X$ composites, an analysis of the peak areas associated with Ag^+ and Ag^0 in the Ag 3d high-resolution XPS spectra for 6AAT, 6.5AAT, 7AAT, 7.5AAT, and 8AAT composites was conducted. The results were compiled in Table 2. The peak area ratios of Ag^0 to Ag^+ for these composites were as follows: 1 : 3.22 (6AAT), 1 : 3.07 (6.5AAT), 1 : 2.98 (7AAT), 1 : 2.88 (7.5AAT), and 1 : 2.70 (8AAT). This data elucidated that with increasing Ag_2S loading, there was a concomitant rise in the peak areas corresponding to both Ag^+ and Ag^0. The Ag^0 content, relative to the $Ag/Ag_2S/Ti_3C_2T_X$ composites, escalated in tandem with heightened Ag_2S loading. This phenomenon underscored that throughout the synthesis of the $Ag/Ag_2S/Ti_3C_2T_X$ composites, a subset of Ag ions became attached to the $Ti_3C_2T_X$ surface. Upon illumination, these surface-adsorbed Ag ions underwent reduction to yield Ag^0, and a greater generation of Ag^0 *via* photoreduction when an increased number of Ag ions were adsorbed onto the $Ti_3C_2T_X$ substrate with Ag_2S loading amplified.

Table 2 Peak area and peak area ratio of Ag^+ and Ag^0 in $Ag/Ag_2S/Ti_3C_2T_X$ composites from Ag 3d high-resolution XPS

Samples	Ag^0 peak area	Ag^+ peak area	Ag^0/Ag^+ peak area ratio
6AAT	6477.5	20910.6	1 : 3.22
6.5AAT	7530.8	23183.7	1 : 3.07
7AAT	8414.5	25127.4	1 : 2.98
7.5AAT	9516.4	27434.4	1 : 2.88
8AAT	10 726	28984.7	1 : 2.70

3.2 Photoelectric property of $Ti_3C_2T_X$ and $Ag/Ag_2S/Ti_3C_2T_X$ composites

To investigate the optical absorption characteristics of the synthesized catalyst materials, an ultraviolet-visible infrared diffuse reflection analysis was conducted on Ag_2S, $Ti_3C_2T_X$, and $Ag/Ag_2S/Ti_3C_2T_X$ composites. As depicted in Fig. 3a, the primary light absorption spectrum of the fabricated semiconductor photocatalyst material predominantly resided within the ultraviolet-visible light domain. Moreover, a partial absorption in the near-infrared region was also observed, suggesting an elevated sunlight utilization efficiency for the material. Both singular materials, Ag_2S and $Ti_3C_2T_X$, exhibiting black coloration, manifest robust light absorption capabilities. Marginal variances in light absorption among the composite materials-specifically 6AAT, 6.5AAT, 7AAT, 7.5AAT, and 8AAT-were discerned, which can be ascribed to the pronounced light absorption intensities inherent to Ag_2S and $Ti_3C_2T_X$ materials. As illustrated in Fig. S3,† by plotting $h\nu$ against $(Ah\nu)^2$ and subsequently determining the intersection point of its external tangent with the abscissa, one can ascertain the band gaps of pristine Ag_2S and $Ti_3C_2T_X$ materials. Notably, the band gaps for pure Ag_2S and $Ti_3C_2T_X$ materials were empirically determined to be 0.86 eV and 1.26 eV, respectively. To ascertain the positions of the conduction bands for the Ag_2S and $Ti_3C_2T_X$ semiconductor materials, Mott–Schottky measurements were executed on both substances. As depicted in Fig. 3b, the flat band potentials (V_{fb}) for Ag_2S and $Ti_3C_2T_X$ were observed to be

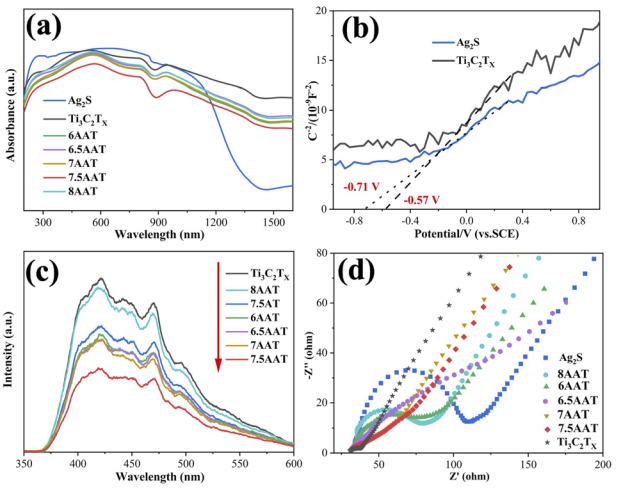

Fig. 3 UV-vis absorbance spectra (a) of Ag_2S, $Ti_3C_2T_X$, and $Ag/Ag_2S/Ti_3C_2T_X$ composites. Mott–Schottky curves (b) obtained on Ag_2S and $Ti_3C_2T_X$. (c) PL spectra and (d) EIS Nyquist plots of Ag_2S, $Ti_3C_2T_X$, and $Ag/Ag_2S/Ti_3C_2T_X$ composites.

−0.71 V and −0.57 V relative to the SCE, respectively. To convert the SCE reference potential to the NHE reference potential, you can use the following formula:

$$E_{\text{fb (vs. NHE)}} = E_{\text{fb (vs. SCE)}} + E^0 + 0.059\ \text{pH} \quad (1)$$

where E^0 (the potential difference between the SCE and NHE reference electrodes at standard conditions) is 0.2415 V and pH is 0. Pertinent literature indicated that both Ag_2S and $Ti_3C_2T_X$ materials were characterized as n-type semiconductors.[25,42–44] For n-type semiconductors, the conduction band potential is more negative compared to the flat band potential, typically by around 0.1 eV.[45,46] Subsequent computations revealed that the conduction band potentials for Ag_2S and $Ti_3C_2T_X$ materials were equivalent to −0.57 and −0.43 V relative to NHE, respectively. Utilizing ultraviolet-visible infrared diffuse reflection analysis, the inherent band gaps of pristine Ag_2S and $Ti_3C_2T_X$ materials were determined to be 0.86 eV and 1.26 eV, respectively. Using the following equation:

$$E_{\text{VB}} = E_{\text{CB}} + E_{\text{g}} \quad (2)$$

where E_{VB} is the valence band, E_{CB} is conduction band bottom, and E_g is the band gap. The valence bands of Ag_2S and $Ti_3C_2T_X$ were deduced to be 0.29 and 0.83 V, respectively.

Fig. 3c presented the fluorescence emission spectra for $Ti_3C_2T_X$ and various $Ag/Ag_2S/Ti_3C_2T_X$ composites, all measured at an emission wavelength of 370 nm. Pristine $Ti_3C_2T_X$ exhibited the highest fluorescence intensity. However, upon modification with Ag/Ag_2S, there was a diminishment in the fluorescence intensity of the resultant composites. This reduction suggested that the Ag/Ag_2S modification effectively hinders the recombination of electron–hole pairs in $Ti_3C_2T_X$. Furthermore, the variation in fluorescence intensity among the composites, each modified with differing amounts of Ag/Ag_2S, implied disparities in the separation velocities of photoinduced charges, contingent upon the Ag_2S loading. Upon the introduction of a minimal quantity of Ag/Ag_2S, there was a notable diminution in fluorescence intensity. This outcome was attributed to the presence of heterojunctions that inhibit the recombination of photogenerated carriers. Conversely, when the Ag/Ag_2S loading surpassed an optimal threshold, superfluous Ag/Ag_2S became polyvalent on the $Ti_3C_2T_X$ substrate. This accumulation engendered sited that facilitate the recombination of electron–hole pairs, leading to an elevation in fluorescence intensity.[29,31,34] Notably, the composite designated as 7.5AAT manifested the most diminished fluorescence intensity, underscoring its superior efficacy in separating electron–hole pairs. In parallel, the 7.5AT composite, devoid of metallic Ag, exhibited fluorescence intensity inferior to that of pristine $Ti_3C_2T_X$ yet exceeding that of 7.5AAT. This juxtaposition substantiated that photoinduced electrons within the composite were conveyed towards the metal Ag, characterized by its low Fermi level. Such migration impeded the reunification of photoinduced electron–hole pairs, wherein the metallic Ag functions as an electron sink within the composite matrix.

Fig. 3d illustrated the alternating current (AC) impedance curve for the synthesized material. Compared with pristine Ag_2S, a notable reduction in the AC impedance arc radius was observed for the 6AAT, 6.5AAT, 7AAT, 7.5AAT, and 8AAT composites. This diminution suggested that the modification of $Ti_3C_2T_X$ with Ag/Ag_2S enhanced the velocity of photogenerated electron migration, thereby facilitating efficient transport of photoinduced carriers. Intriguingly, the $Ti_3C_2T_X$ substrate, inherently characterized by superior electrical conductivity, manifested the smallest AC impedance arc radius, correlating with the most rapid migration of photo-induced carriers. A subsequent analytical perspective revealed that the AC impedance arc radii for the 6AAT, 6.5AAT, 7AAT, 7.5AAT, and 8AAT composites initially diminish and then subsequently augment. This trend delineated that at a lower Ag/Ag_2S loading, the carriers, upon photoexcitation, could be expeditiously conveyed and partitioned *via* the heterojunction. In instances where the Ag/Ag_2S loading surpasses an optimal threshold, consequently forming a recombination center for Ag/Ag_2S tended to polymerize on the sample surface, photogenerated carriers, thereby impeding carrier migration. As depicted in Fig. S4,† it presented a transient photocurrent test plot for the synthesized materials. Notably, the current intensity exhibited by 7.5AAT is higher than that of pristine Ag_2S and $Ti_3C_2T_X$. Cumulatively, these findings substantiated that the $Ag/Ag_2S/Ti_3C_2T_X$ composite adeptly facilitated the separation of photo-induced electron–hole pairs. Moreover, the incorporation of metallic Ag augmented the propagation speed of photogenerated electrons, concomitantly elevating the photocatalytic efficacy of the $Ag/Ag_2S/Ti_3C_2T_X$ composite.

3.3 Photocatalytic reduction of CO_2 over $Ag/Ag_2S/Ti_3C_2T_X$ composites

To evaluate the photoreduction efficacy of various photocatalytic materials towards CO_2, an assessment of the photocatalytic activities of the synthesized materials was conducted. As illustrated in Fig. 4a and b, the primary products derived from the photocatalytic reduction of CO_2 were identified as methanol and ethanol. Subsequent to a 4 hours photocatalytic reduction reaction employing substrates such as $Ti_3C_2T_X$, Ag_2S, 7.5AT, 6AAT, 6.5AAT, 7AAT, 7.5AAT, and 8AAT composites, the resultant methanol yields manifested an initial ascending trend, followed by a descending pattern. Specifically, the methanol yields were recorded as 37.6, 14.7, 61.3, 73.5, 87.1, 90.8, 107.4, and 68.7 μmol $g_{catal.}^{-1}$, respectively. Conversely, ethanol production exhibited an initial rise, followed by a decline, and subsequently stabilized at consistent yields, with values measured at 23.1, 10.0, 27.9, 28.2, 17.8, 19.3, 17.9, and 19.7 μmol $g_{catal.}^{-1}$, correspondingly. Notably, the 7.5AAT substrate demonstrated superior performance, achieving the highest cumulative yield of 125.3 μmol $g_{catal.}^{-1}$, which was approximately 5.1-fold greater than the aggregate yields of Ag_2S (24.7 μmol $g_{catal.}^{-1}$). Additionally, an evaluation of the photocatalytic reduction capability of the 7.5AT substrate devoid of metallic Ag was undertaken, revealing a methanol yield of 61.3 μmol $g_{catal.}^{-1}$, an ethanol yield of 27.9 μmol $g_{catal.}^{-1}$, and a cumulative yield of 89.2 μmol $g_{catal.}^{-1}$. This data indicated that the overall production of the 7.5AAT composite was 1.4 times

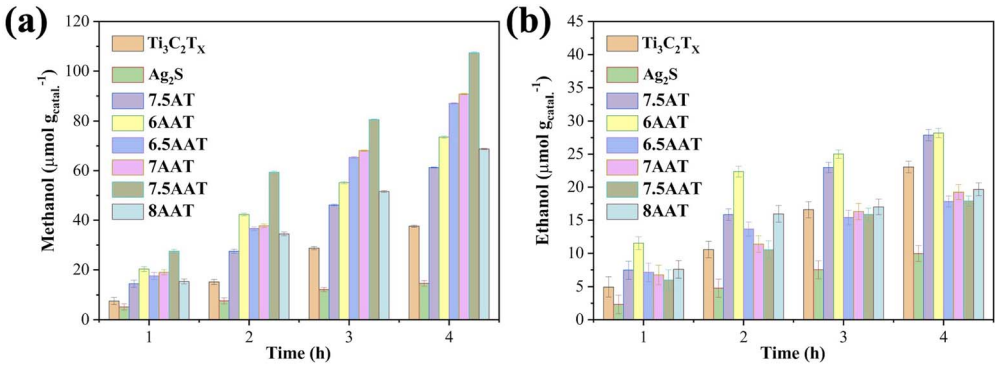

Fig. 4 Yields of (a) methanol and (b) ethanol from photocatalytic CO_2 reduction over Ag_2S, $Ti_3C_2T_X$, and $Ag/Ag_2S/Ti_3C_2T_X$ composites with increasing irradiation time under visible light.

greater than that of the 7.5AT composite. The cycling stability of CO_2 reduction over 7.5AAT was inspected in Fig. S5.† The total yield of methanol and ethanol obtained using 7.5AAT in five cycles are 125.30, 120.17, 115.87, 111.46 and 109.48 μmol $g_{catal.}^{-1}$, respectively. The performance over 7.5AAT represents little decrease after five cycling runs, but the 7.5AAT exhibited unchanged morphology and crystal structure after tests (Fig. S6†). Such findings suggested that Ag functions as both an electron acceptor and an active site within the $Ag/Ag_2S/Ti_3C_2T_X$ composite, thereby enhancing the photocatalytic reduction of CO_2. Given the aforementioned experimental outcomes, coupled with comprehensive material characterization and analytical assessment, several factors contributing to the elevated photocatalytic efficacy of the $Ag/Ag_2S/Ti_3C_2T_X$ composite can be identified. Primarily, the inherent conductivity and rapid electron transit characteristics of the $Ti_3C_2T_X$ layered substrate are noteworthy. Secondly, the elevated energy at the sulfide conduction band edge amplifies, and the reduction potential of electrons residing on the Ag_2S conduction band is particularly favorable for CO_2 reduction. Moreover, the incorporation of metallic Ag, characterized by its low Fermi level within the composite matrix, facilitates its role as an electron acceptor and reaction locus. Photoexcited electrons, originating from both Ag_2S and $Ti_3C_2T_X$, are shuttled to metallic Ag *via* the heterojunction, subsequently engaging with adsorbed CO_2 molecules. This mechanism not only amplifies the number of electrons participating in the photocatalytic reduction but also enhances the overall photocatalytic efficiency. However, it is crucial to modulate the quantity of Ag/Ag_2S judiciously because an excess may result in the aggregation of Ag and Ag_2S on the $Ti_3C_2T_X$ layered surface. Such aggregation can impede the efficient separation of photoinduced electron–hole pairs, adversely impacting the photocatalyst performance of the material to a certain extent.

3.4 Proposed mechanism involved in CO_2 photoreduction over $Ag/Ag_2S/Ti_3C_2T_X$ composites

The examination of experimental outcomes revealed a notable enhancement in the catalytic efficacy of the $Ag/Ag_2S/Ti_3C_2T_X$ composite towards the photoreduction of CO_2. The reduction mechanism is depicted in Fig. 5. The improvement of photocatalytic efficiency can be attributed to three primary factors. First, the layered $Ti_3C_2T_X$ possesses superior electrical conductivity, thereby augmenting the transit of photoinduced electrons, which in turn facilitates the segregation of electrons and holes to a discernible extent. Second, the Ag_2S conduction band is particularly amenable to CO_2 reduction to give the pronounced reducing capability of photoinduced electrons on the sulfide conduction band. Concurrently, the formation of a heterojunction between Ag_2S and $Ti_3C_2T_X$ further encourages the segregation of electron–hole pairs. Moreover, the presence of metallic Ag, characterized by its low Fermi level, enables it to function as an electron sink and active reaction site. Photoinduced electrons generated by the composite are shunted to Ag, where they engage with the surface-adsorbed CO_2, leading to a commensurate increase in photoreduction efficacy. The energy levels associated with the valence band, conduction band and forbidden band of Ag_2S and $Ti_3C_2T_X$ can be determined utilizing ultraviolet-visible infrared diffuse reflection spectroscopy and Mott–Schottky analysis. By semiconductor

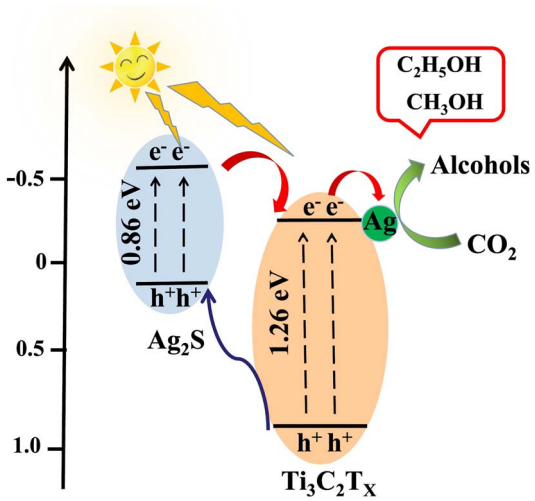

Fig. 5 Schematic diagram of bandgap structure and photocatalytic CO_2 reduction over $Ag/Ag_2S/Ti_3C_2T_X$ composites.

photocatalysis principles, upon exposure to light irradiation, both Ag_2S and $Ti_3C_2T_X$ produce photo-induced charge carriers. These include photo-induced electrons, which exhibit potent reducing capabilities, and photo-induced holes, known for their robust oxidizing effects. The establishment of heterojunctions facilitates the transfer of photo-induced electrons from semiconductor materials possessing a more electronegative conduction band to those with a less electronegative conduction band. Simultaneously, photo-induced holes transition from semiconductors with a higher valence band to those with a lower valence band, thereby inhibiting the recombination of photo-induced charge carriers. In essence, metallic Ag functions as an electron sink and provides an active reaction site. Photo-induced electrons, originating from Ag_2S and $Ti_3C_2T_X$ upon photoexcitation, not only engage in the photoreduction process but are also channeled to metallic Ag *via* the heterojunction, facilitating the reduction of CO_2 adsorbed onto the material's surface. The resultant $Ag/Ag_2S/Ti_3C_2T_X$ composite effectively curtails the recombination of photo-induced electron–hole pairs, prolonging the lifespan of the photo-induced carriers.

4 Conclusions

In this study, $Ag/Ag_2S/Ti_3C_2T_X$ heterojunction composites were synthesized by integrating coprecipitation and photoreduction techniques, wherein Ag/Ag_2S was loaded onto the layered $Ti_3C_2T_X$. Upon photoexcitation, both Ag_2S and $Ti_3C_2T_X$ materials generated photo-induced carriers. The conduction band of Ag_2S was more electronegative than that of $Ti_3C_2T_X$, leading to the transfer of photo-induced carriers from Ag_2S to the $Ti_3C_2T_X$ substrate *via* the heterojunctions. Owing to the substantial presence of photoproduced Ag on $Ti_3C_2T_X$ and the low Fermi level of Ag, the photogenerated electrons on $Ti_3C_2T_X$ were shuttled to Ag particles. This mechanism effectively inhibited the recombination of electron–hole pairs and enhanced CO_2 photocatalytic reduction efficiency. Additionally, metallic Ag improved photogenerated electrons migration efficiency and prolonged carrier lifespan, acting as an active site in the photocatalytic reaction. $Ag/Ag_2S/Ti_3C_2T_X$ heterojunction thus significantly improved CO_2 photoreduction performance, as evidenced by the increased yields of methanol and ethanol. This work offers valuable insights for designing intimate heterostructures that enable effective photogenerated carrier separation and full spectral absorption, thereby enhancing photocatalytic CO_2 reduction.

Data availability

The data that support the findings of this study are available from the corresponding author upon request.

Author contributions

F. L., W. X., and B. Z. conceived the idea and supervised the entire project. W. X., W. D., and Y. Z. designed the methodology and conducted the experiments. X. L., B. Z., and W. D. analyzed the data and visualized the data. F. L. and Y. C. wrote the manuscript. B. Z. contributed to funding support. F. L., W. X., and B. Z. commented on or edited the manuscript.

Conflicts of interest

There are no conflicts to declare.

Acknowledgements

This work is supported by the National Natural Science Foundation of China (22406208), the Zhaoqing City Science and Technology Innovation Guidance Project (No. 2023040304001), the Zhaoqing University High-level Project Cultivation Program (GCCZK202416), the Zhaoqing University Doctor Start-up Fund (240016) and Zhaoqing University Teaching Reform Project (zlgc2024060).

References

1 S. Zhou, P. Huang, L. Wang, K. Hu, G. Huang and P. Hu, *Nat. Commun.*, 2024, **15**, 96.
2 Y. Chen, W. Qin, Q. Zhang, X. Wang, J. Feng, M. Han, Y. Hou, H. Zhao, Z. Zhang, J.-S. He, M. S. Torn and B. Zhu, *Nat. Commun.*, 2024, **15**, 4489.
3 R. Zhang, Z. Liu, D. Jiang, Y. Yu, Z. Zhang, Y. Yang, N. Tan, D. Si, Q. Zhang and X. Zhou, *Sci. Bull.*, 2024, **69**, 1323–1331.
4 A. Goeppert, M. Czaun, J.-P. Jones, G. K. Surya Prakash and G. A. Olah, *Chem. Soc. Rev.*, 2014, **43**, 7995–8048.
5 K. Meeran, N. Verbrigghe, J. Ingrisch, L. Fuchslueger, L. Müller, P. Sigurðsson, B. D. Sigurdsson, H. Wachter, M. Watzka, J. L. Soong, S. Vicca, I. A. Janssens and M. Bahn, *Global Change Biol.*, 2023, **29**, 5276–5291.
6 W. Zhao, Q. Ge, H. Li, N. Jiang, S. Chen, S. Yang and H. Cong, *Polym. Chem.*, 2023, **14**, 4877–4889.
7 K.-G. Liu, F. Bigdeli, A. Panjehpour, A. Larimi, A. Morsali, A. Dhakshinamoorthy and H. Garcia, *Coord. Chem. Rev.*, 2023, **493**, 215257.
8 J. Hu, J. Ma, Q. Zhu, Q. Qian, H. Han, Q. Mei and B. Han, *Green Chem.*, 2016, **18**, 382–385.
9 J. A. Church and N. J. White, *Surv Geophys*, 2011, **32**, 585–602.
10 I. Omae, *Coord. Chem. Rev.*, 2012, **256**, 1384–1405.
11 F. Galli, M. Compagnoni, D. Vitali, C. Pirola, C. L. Bianchi, A. Villa, L. Prati and I. Rossetti, *Appl. Catal., B*, 2017, **200**, 386–391.
12 X. Chang, T. Wang and J. Gong, *Energy Environ. Sci.*, 2016, **9**, 2177–2196.
13 S. Cao, B. Shen, T. Tong, J. Fu and J. Yu, *Adv. Funct. Mater.*, 2018, **28**, 1–11.
14 Q. Tang, T. Li, W. Tu, H. Wang, Y. Zhou and Z. Zou, *Adv. Funct. Mater.*, 2024, **34**, 1–21.
15 T. P. Nguyen, D. M. Tuan Nguyen, D. L. Tran, H. K. Le, D.-V. N. Vo, S. S. Lam, R. S. Varma, M. Shokouhimehr, C. C. Nguyen and Q. Van Le, *Mol. Catal.*, 2020, **486**, 110850.
16 J. O. Ighalo, M. L. Smith, A. Al Mayyahi and P. B. Amama, *Appl. Catal. B*, 2024, **358**, 124352.

17 J. Nie, X. Zhang, M. Wang, Y. Ou, S. Li, P. Zhong, W. Wang, G. Zhu and X. Ma, *Sep. Purif. Technol.*, 2025, **354**, 128961.
18 C. Peng, X. Yang, Y. Li, H. Yu, H. Wang and F. Peng, *ACS Appl. Mater. Interfaces*, 2016, **8**, 6051–6060.
19 Y.-J. Yuan, P. Wang, Z. Li, Y. Wu, W. Bai, Y. Su, J. Guan, S. Wu, J. Zhong, Z.-T. Yu and Z. Zou, *Appl. Catal., B*, 2019, **242**, 1–8.
20 S. Huang, C. Chen, H. Tsai, J. Shaya and C. Lu, *Sep. Purif. Technol.*, 2018, **197**, 147–155.
21 F. A. Frame and F. E. Osterloh, *J. Phys. Chem. C*, 2010, **114**, 10628–10633.
22 X. Zong, H. Yan, G. Wu, G. Ma, F. Wen, L. Wang and C. Li, *J. Am. Chem. Soc.*, 2008, **130**, 7176–7177.
23 D. Ruiz, B. del Rosal, M. Acebrón, C. Palencia, C. Sun, J. Cabanillas-González, M. López-Haro, A. B. Hungría, D. Jaque and B. H. Juarez, *Adv. Funct. Mater.*, 2017, **27**, 1604629.
24 Z. Lou, S. Kim, M. Fujitsuka, X. Yang, B. Li and T. Majima, *Adv. Funct. Mater.*, 2018, **28**, 1–9.
25 U. Jadhav and M. Shinde, *J. Res. Chem.*, 2023, **4**, 69–73.
26 D. Jiang, L. Chen, J. Xie and M. Chen, *Dalton Trans.*, 2014, **43**, 4878–4885.
27 S. I. Sadovnikov, E. A. Kozlova, E. Y. Gerasimov and A. A. Rempel, *Catal. Commun.*, 2017, **100**, 178–182.
28 W. Hu, L. Zhao, Y. Zhang, X. Zhang, L. Dong, S. Wang and Y. He, *J. Exp. Nanosci.*, 2016, **11**, 433–444.
29 X. Chen, F. Liu, X. Yan, Y. Yang, Q. Chen, J. Wan, L. Tian, Q. Xia and X. Chen, *Chem.–Eur. J.*, 2015, **21**, 18711–18716.
30 J. Liu, L. Jing, G. Gao, Y. Xu, M. Xie, L. Huang, H. Ji, J. Xie and H. Li, *RSC Adv.*, 2017, **7**, 46823–46831.
31 W. Xiong, W. Dai, X. Hu, L. Yang, T. Wang, Y. Qin, X. Luo and J. Zou, *Mater. Lett.*, 2018, **232**, 36–39.
32 J. He, Y. Cheng, T. Wang, D. Feng, L. Zheng, D. Shao, W. Wang, W. Wang, F. Lu, H. Dong, R. Zheng and H. Liu, *Appl. Surf. Sci.*, 2018, **440**, 99–106.
33 W. Jiang, Z. Wu, Y. Zhu, W. Tian and B. Liang, *Appl. Surf. Sci.*, 2018, **427**, 1202–1216.
34 S. Zhang, W. Xiong, J. Long, Y. Si, Y. Xu, L. Yang, J. Zou, W. Dai, X. Luo and S. Luo, *J. Colloid Interface Sci.*, 2022, **615**, 716–724.
35 C. Peng, H. Wang, H. Yu and F. Peng, *Mater. Res. Bull.*, 2017, **89**, 16–25.
36 A. K. Singh, K. Mathew, H. L. Zhuang and R. G. Hennig, *J. Phys. Chem. Lett.*, 2015, **6**, 1087–1098.
37 X. Wang, K. Maeda, A. Thomas, K. Takanabe, G. Xin, J. M. Carlsson, K. Domen and M. Antonietti, *Nat. Mater.*, 2009, **8**, 76–80.
38 M. Pang, J. Hu and H. C. Zeng, *J. Am. Chem. Soc.*, 2010, **132**, 10771–10785.
39 S. Das Chakraborty, U. Kumar, P. Bhattacharya and T. Mishra, *ACS Appl. Mater. Interfaces*, 2024, **16**, 2204–2215.
40 H. Zhang, L. Ma, J. Ming, B. Liu, Y. Zhao, Y. Hou, Z. Ding, C. Xu, Z. Zhang and J. Long, *Appl. Catal., B*, 2019, **243**, 481–489.
41 M. Basu, R. Nazir, C. Mahala, P. Fageria, S. Chaudhary, S. Gangopadhyay and S. Pande, *Langmuir*, 2017, **33**, 3178–3186.
42 Z. Yang, H. Zou, Y. Zhang, F. Liu, J. Wang, S. Lv, L. Jiang, C. Wang, X. Yan, P. Sun, L. Zhang, Y. Duan and G. Lu, *Adv. Funct. Mater.*, 2022, **32**, 2108959.
43 Y. Yan, R. Yu, C. Gao, Y. Sui, Y. Deng, H. Chen and T. Guo, *Sci. China Mater.*, 2022, **65**, 3087–3095.
44 W. Dai, W. Xiong, J. Yu, S. Zhang, B. Li, L. Yang, T. Wang, X. Luo, J. Zou and S. Luo, *ACS Appl. Mater. Interfaces*, 2020, **12**, 25861–25874.
45 J. Zhang, X. Chen, K. Takanabe, K. Maeda, K. Domen, J. D. Epping, X. Fu, M. Antonietti and X. Wang, *Angew. Chem., Int. Ed.*, 2010, **49**, 441–444.
46 J. Wang, Y. Yu and L. Zhang, *Appl. Catal., B*, 2013, **136–137**, 112–121.